Effects of offshore fringing reefs on the transient harbor resonance excited by solitary waves

Junliang Gao [1, 2, 3], Xiaozhou Ma [2 *], Guohai Dong [2], Jun Zang [3], Yuxiang Ma [2], Li Zhou [1]

1. School of Naval Architecture and Ocean Engineering, Jiangsu University of Science and Technology, Zhenjiang 212003, China.

2. State Key Laboratory of Coastal and Offshore Engineering, Dalian University of Technology, Dalian 116024, China.

3. Research Unit for Water, Environment and Infrastructure Resilience (WEIR), Department of Architecture and Civil Engineering, University of Bath, BA2 7AY, U.K.

Abstract

In this article, effects of the variation of the offshore reef topography on the transient resonance induced by solitary waves with various wave heights are first investigated. The transient resonance is simulated by a fully nonlinear Boussinesq model, FUNWAVE-TVD. This paper focuses on investigating how the variations of the plane reef-face slope, the reef-ridge width, the lagoon width and the reef-face profile shape affect the wave energy distribution, the total wave energy and the maximum oscillation (runup) inside the harbor. Results indicate that all of the uniformity of the wave energy distribution, the total wave energy and the amplification factor of the incident solitary wave (defined as the ratio of the maximum runup to the incident wave height) are shown to gradually decrease with the plane reef-face slope. For the other three topographical parameters (i.e., the reef-ridge width, the lagoon width and the reef-face profile shape), their influences on the resonant wave parameters inside the harbor becomes more complicated. Not all of the resonant wave parameters inside the harbor (i.e., the uniformity of the wave energy distribution, the total wave energy and the amplification factor of the incident solitary wave) present monotonic changes with these three topographical parameters.

Key words:

Harbor resonance; Harbor oscillations; Fringing-reef topography; Numerical simulations;

*Corresponding author. Tel.: +86 411 8470 7262; fax: +86 411 847 08526. E-mail address: maxzh@dlut.edu.cn.

Boussinesq equations; FUNWAVE-TVD

1. Introduction

Harbor resonance (also termed as *harbor oscillations*) is the phenomenon of the trapping and amplification of wave energy inside a semi-enclosed water body (e.g., a bay or a harbor). It may be excited by tsunamis, wave groups, infra-gravity waves, atmospheric fluctuations and shear flow (Bellotti et al., 2012; De Jong and Battjes, 2004; Dong et al., 2013; Fabrikant, 1995; Gao et al., 2016a; Liu et al., 2003; Okihiro and Guza, 1996). By creating significant vessel movements, harbor oscillations may interrupt the operation of wharfs and cause excessive mooring forces which could even break mooring lines (Kumar et al., 2016; López and Iglesias, 2014).

Among various induced mechanisms, harbor resonance excited by tsunamis often have destructive effects. Tsunamis are triggered by undersea volcanic eruptions, submarine earthquakes, offshore landslides, or other types of disturbances (e.g., onshore landslides falling into water). As tsunamis propagate into the coastal zone, their wave heights obviously increases because of the continuous decrease of the water depth (Zhao et al., 2012). For example, the Indian Ocean tsunami, which was triggered by the Sumatra earthquake on 26th December, 2004, travelled for around two hours to Colombo harbor (Sri Lanka) and induced extreme resonance with a period of 75 min and a maximum wave height of 3.87 m (Pattiaratchi and Wijeratne, 2009). Hence, it is essential to carry out further research efforts to enhance our current understanding for this kind of wave amplification and thus improve our prediction ability.

Although the research on harbor resonance started from the early 1950s (Vanoni and Carr, 1950), most of the past investigations have been confined to stationary harbor oscillations excited by the steady wave fields [e.g., Gao et al. (2019); Gao et al. (2018c); Kumar and Gulshan (2018); Lee (1971); Mei and Agnon (1989); Vanoni and Carr (1950); Wang et al. (2013); Wang et al. (2014)]. The investigation on transient harbor oscillations triggered by transient long waves began relatively late and few scholars devoted to this problem. Based on both analytical and experimental methods, Lepelletier and Raichlen (1987) investigated nonlinear transient oscillations inside the harbor excited by transient long waves, such as tsunamis. By combining laboratory experiments with Boussinesq equation-based simulations, Dong et al. (2010) studied the response of an elongated harbor to the impact waves triggered by subaerial landslide. It was found that the impact waves with

solitary wave characteristics play a decisive role in the harbor resonance. Recently, by using a fully nonlinear Boussniesq model, Gao et al. (2016b; 2016c) performed investigations on the transient harbor resonance induced by solitary waves. More recently, the transient harbor oscillations induced by other two types of tsunami waveforms (i.e., N-waves and successive solitary waves) were further investigated by Gao et al. (2017a; 2018a).

The vast majority of the coastlines in the world, perhaps up to 80%, comprise a broad category of submersed offshore reef structures, which include relic temperate limestone platforms, tropical coral reefs and rocky coastal features (Dongeren et al., 2013). Hence, in the last few decades, the interactions between waves and fringing reefs have become one of the primary concerns in the fields of coastal and offshore engineering (Ma et al., 2017; Yao et al., 2016). A typical fringing reef is characterized by a seaward sloping reef face and an inshore shallow reef flat extending toward the coastline. Reef ridges have been observed frequently at the edges of fringing reefs even though their profiles may vary from site to site (Yao et al., 2012).

The influences of offshore reef topography on harbor oscillations have already been concerned by some researchers. Based on field measurements around Two Rocks Marina of Australia and numerical simulations of a Boussinesq model, Thotagamuwage and Pattiaratchi (2014a, b) found that the infragravity wave energy over the offshore reefs can be increased by 8–10 times compared to that at offshore, and that the increased infragravity wave energy over the reefs significantly intensifies the infragravity-period oscillations inside the marina. Recently, based on numerical simulations, Gao et al. (2017b; 2017c; 2018b; 2019) investigated the effects of offshore reef topographical variation on the infragravity-period harbor oscillations induced by wave groups. The offshore reef topographical variation considered in their papers includes various plane reef-face slopes, reef-face profile shapes and whether reef ridge exists or not.

However, to the best of the authors' knowledge, so far, the investigations on the influence of the offshore reef topography on harbor oscillations are restricted to the steady-state oscillations excited by incident wave groups (e.g., Gao et al. (2017b; 2017c; 2018b; 2019)), and how the offshore reef topography affects the transient harbor oscillations induced by transient long waves, such as tsunamis, has not been reported in the literature. In order to broaden the understanding of tsunami-induced oscillations, this paper utilizes solitary waves to further explore the effects of offshore reef topography on the transient harbor oscillations. The main focus of this article is to systematically

investigate the effects of offshore reef topographical variation (including different plane reef-face slopes, widths of the reef ridge and the lagoon and reef-face profile shapes) on the wave energy distribution and the total wave energy inside the harbor during transient oscillations excited by normal-incident solitary waves with various wave heights. The maximum oscillations (runups) of the incident solitary waves inside the harbor are also studied. In this article, all numerical simulations are carried out utilizing a fully nonlinear Boussinesq model, FUNWAVE-TVD (Shi et al., 2012). For simplification, the harbor is assumed to be long and narrow, and has a flat bottom; the free surface movement inside the harbor then essentially becomes one-dimensional.

The remainder of the paper is organized as follows: Section 2 describes the numerical model and the data analysis technique. The applicability of the former over rapidly varying bathymetry will be verified by a set of numerical simulations. Section 3 presents the numerical wave tank setup and the incident wave parameters. Section 4 demonstrates the simulation results, which are explained in detail. Concluding remarks based on the results are given in Section 5.

2. **Numerical model and data analysis technique**

2.1. Numerical model

2.1.1. Model description

This section presents a brief introduction to the fully nonlinear Boussinesq model, FUNWAVE-TVD, developed by Shi et al. (2012). Using a hybrid finite volume-finite difference scheme, the fully nonlinear Boussinesq equations of Chen (2006) are solved, and a moving reference level as in Kennedy et al. (2001) is also incorporated in the model. To simulate wave breaking and associated wave energy dissipation without relying on empirical formulations, a high-order shock-capturing Total Variation Diminishing (TVD)-type scheme is adopted to solve the control equations (Ma et al., 2012; Shi et al., 2012). In addition, a robust wetting-drying scheme is utilized to capture the moving shoreline, and a third-order Strong Stability Preserving (SSP) high order Runge-Kutta scheme is used for adaptive time stepping. The Message Passing Interface (MPI) is used to parallelize the model with non-blocking communication. With these improvements, it has been proved to be more robust on the prediction of wave processes in the nearshore, which includes wave shoaling, diffraction, refraction, wave breaking as well as wave runup/rundown on beaches (Ning et al., 2019; Shi et al., 2012; Su et al., 2015).

2.1.2. Model validation for rapidly varying bathymetry

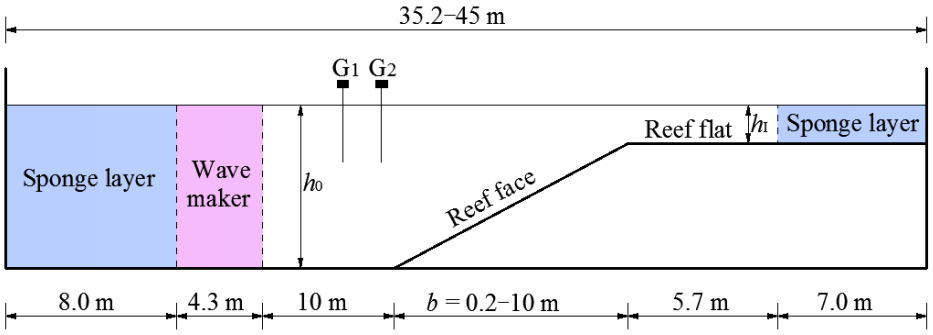

Fig. 1. Sketch of the numerical wave tank used in testing simulations (the incident waves propagate from left to right).

Different from normal coastal beaches, which usually have mild slopes, a typical fringing reef often contains a sharp transition from the relatively deep water to shallow water. One of the main concerns when utilizing Boussinesq wave models to fringing reefs is the relatively steep reef-face slopes. This is due to the fact that some higher-order derivative terms of the water depth are abandoned during the derivation process of the control equations of Boussinesq models.

To examine the capability of FUNWAVE-TVD to handle rapidly changing bathymetry, a train of regular waves propagating over plane reef faces with various slopes are simulated here. The problem was first studied by Booij (1983) to verify the accuracy of a mild-slope equation through comparison of the estimated reflection coefficient and a finite element method (FEM) solution based on the linear potential wave theory. However, Booij (1983)'s FEM solution only considered the slope range larger than around 1:3, and there is no data for the milder slopes. Then, also based on the linear potential wave theory, Booij (1983)'s FEM solution was expanded to the milder slopes by Suh et al. (1997). Subsequently, Madsen et al. (2006), Yao et al. (2012) and Gao et al. (2017b) reproduced this problem to verify the ability of their respective Boussinesq models. The sketch of the bottom profile for this problem is illustrated in Fig. 1, which includes a plane slope connecting two constant-depth regions. The water depth at the open sea, h_0, and that over the reef flat, h_I, are set to 0.6 m and 0.2 m, respectively. A train of regular waves with a period of T=2.0 s are generated at the wave-maker zone. The reef-face width, b, varies from 10 m to 0.2 m, which corresponds to the slope range of $S=(h_0-h_I)/b$=0.04–2.0. A grid size of 0.02 m is adopted for all simulations. Two

wave gauges, G_1 and G_2, are arranged in front of the reef face to separate the incident and reflected waves, and their distances from the toe of the reef face are 4.36 m and 4.12 m, respectively. Two sponge layers are deployed at the right and left boundaries of the numerical tank to dissipate the incident and reflected waves effectively.

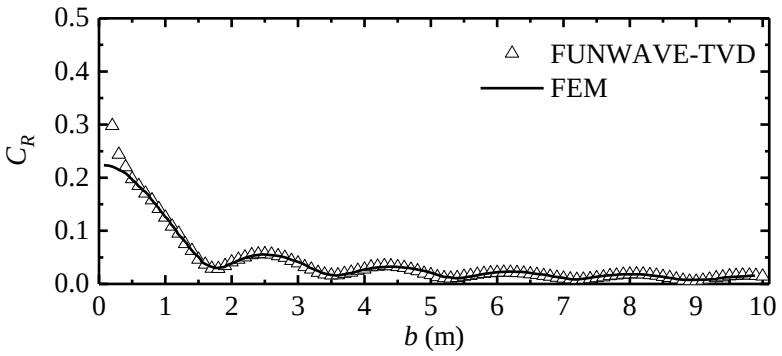

Fig. 2. Comparison of the reflection coefficient, C_R, obtained by FUNWAVE-TVD (triangle) and the FEM solution of Suh et al. (1997) (solid line).

The comparison of the predicted reflection coefficient by the present model and the FEM solution of Suh et al. (1997) is presented in Fig. 2. It is obviously shown that the present numerical results are accurate up to b=0.5 m, i.e., a slope of S=0.8, but distinctly overestimate the reflection coefficients for slopes steeper than 0.8. It is noted that the reflection coefficient presents obvious fluctuation with respect to the reef-face width, b, which can be ascribed to the trapping of the wave energy by reflection over the reef face (Yao et al., 2012).

2.2. Data analysis technique

The wave fields inside the harbor for all the simulations in the current study are analyzed by adopting the normal mode decomposition (NMD) method. This method was originally proposed by Sobey (2006) to predict the eigenfrequencies, eigenmodes and response amplitudes of various resonant modes in natural bays and harbors which are exposed to tsunamis or storm tides. The NMD method includes two calculating steps. The first step calculates the discrete set of eigenfrequencies and associated eigenmodes of the semi-enclosed body of water. The second step involves the estimation of the response amplitudes at the discrete modes. It is formulated and solved as a multi-dimensional optimization problem, in which the eigenfrequencies and eigenmodes predicted in the first step are utilized as known variables. Subsequently, the NMD method was improved by Gao et

al. (2015) so that the prediction of the eigenfrequencies and eigenmodes becomes more accurate. Recently, by adopting this data analysis technique, the wave energy distributions inside the harbor during transient oscillations triggered by different types of tsunamis, including solitary waves, N-waves and successive solitary waves, were comprehensively analyzed in Gao et al. (2017a; 2016b; 2018a). For the detailed theory on the NMD method, the interested reader is referred to Sobey (2006) and Gao et al. (2015).Similar to Gao et al. (2017a; 2016b; 2018a), all numerical simulations in this article also utilize this method to analyze the wave energy distribution inside the harbor excited by incident solitary waves.

3. Numerical setup

Fig. 3 presents the numerical wave tank adopted in the simulations. The wave tank has dimensions of 1600 m by 30 m, and all its boundaries are set to be totally reflective. The harbor has a length of 200 m and a width of 5 m. 201 wave gauges (G_1–G_{201}) are equidistantly deployed along the center line of the harbor with a spacing of 4 m. The length of the reef flat located outside the harbor is set to 200 m (the length of 200 m also includes reef ridge and/or lagoon if they exist). The still water depth both over the reef flat and inside the harbor is a constant and equals h_I=2 m, and the water depth in the open sea is set to h_0=6 m.

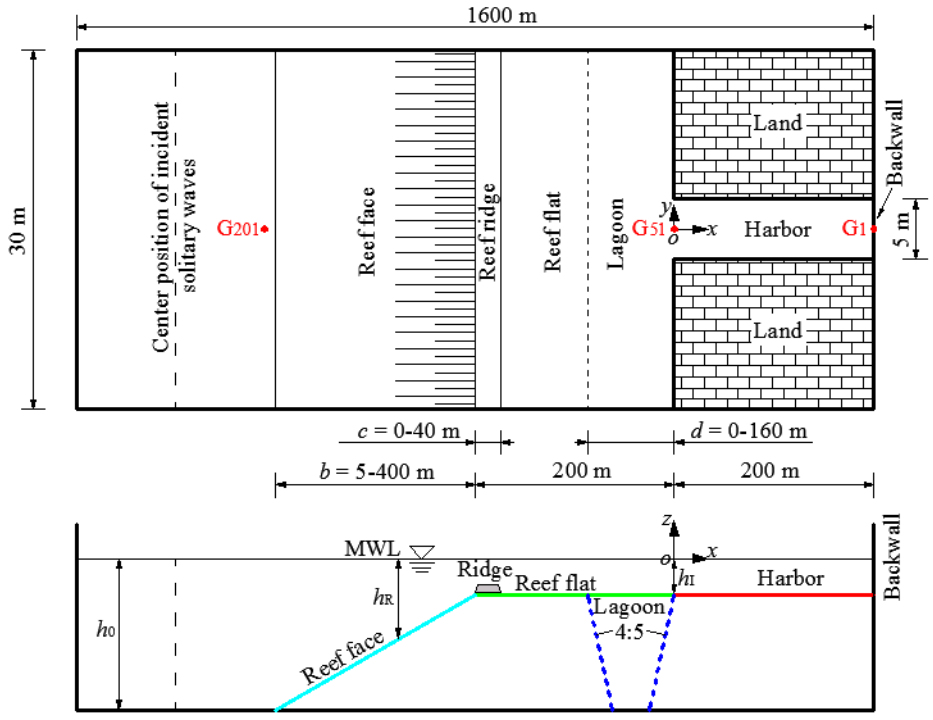

Fig. 3. Sketch of the numerical wave tank. Upper panel: top view; lower panel: longitudinal section at y=0 (taking the reef face with the plane slope for example). Since the wave tank is symmetric with respect to the x-axis, only a half-domain (i.e. $y \geq 0$) is used for computations.

As mentioned in Section 1, the purpose of this article is to study the effects of the following four geometrical parameters on the transient resonant characteristics within the harbor. These four geometrical parameters include the following: (1) the plane reef-face slope, (2) the reef-ridge width, (3) the lagoon width and (4) the reef-face profile shape. The offshore reef topography in all the simulations are designed according to these four geometrical parameters. Firstly, in order to investigate effects of the plane reef-face slope on the transient harbor oscillations, five different reef-face widths (i.e., b=5 m, 100 m, 200 m, 300 m and 400 m) are considered. Meanwhile, both the reef ridge and the lagoon are not taken into consideration here (i.e., c=d=0). It should be noted here that for the plane reef face with b=5–400 m, the slope S varies from 0.8 to 0.01; in this range, the reflection effect of the reef face can be accurately estimated by FUNWAVE-TVD (see Section 2.1.2). Secondly, to study influences of the reef-ridge width, a trapezoidal prism with a length of 30 m and a height of 0.6 m is placed on the reef flat with its front face aligned to the reef edge (x = –200.0 m) to imitate an idealized ridge; the reef-ridge width (i.e., the base width of the prism), c, increases gradually from 0 to 40 m in interval of 10 m. To ensure the numerical stability in simulations, both the leeside and seaside ridge slopes are set S=0.6. Thirdly, to discuss effects of the lagoon width, a deep lagoon with a water depth of 6 m is considered, and the lagoon width, d, varies from 0 to 160 m with an increment of 40 m. The right edge of the lagoon is always aligned to the harbor entrance and the slope of the two sidewalls of the lagoon is set to 4:5. It should be emphasized here that when studying the effects of both the reef-ridge width and the lagoon width, only the cases with the plane reef-face slopes of b=5m, 100 m and 400 m are considered. In addition, these two geometrical parameters are not considered at the same time. In other words, when the effects of the reef-ridge width are investigated, the value of the lagoon width is set to d=0, and vice versa.

To investigate influences of different topographies inside the harbor on transient harbor resonance triggered by solitary waves, Gao et al. (2016b) considered three kinds of topographies, i.e., an arc-tangent-type bottom, a plane slope bottom and a hyperbolic-cosine-type bottom. Enlightened by Gao et al. (2016b), in order to discuss effects of the different reef-face profiles on

transient harbor oscillations, these three kinds of topographies are also used in this article to imitate various reef-face profiles. The local water depth over the reef face can be expressed as

$$h_{\mathrm{R}}(x)=\begin{cases} h_{\mathrm{I}}+\alpha\,\mathrm{atan}\left[\beta\left(x+200\right)\right] & \text{Arc-tangent-type bottom} \\ h_{\mathrm{I}}+S\left(x+200\right) & \text{Plane slope bottom} \\ h_{\mathrm{I}}\cosh^{\kappa}\left[\mu\left(x+200\right)\right] & \text{Hyperbolic-cosine-type bottom} \end{cases}. \tag{1}$$

The symbols α, β, S, κ and μ are the parameters determining the bottom profile of the reef face, and they satisfy the following mathematical relationships:

$$S=\frac{h_{\mathrm{I}}-h_0}{b}, \tag{2}$$

$$\beta=-\frac{1}{b}\tan\left(\frac{h_0-h_{\mathrm{I}}}{\alpha}\right), \tag{3}$$

and

$$\mu=-\frac{1}{b}\mathrm{acosh}\left[\left(\frac{h_0}{h_{\mathrm{I}}}\right)^{1/\kappa}\right]. \tag{4}$$

For both the arc-tangent-type and hyperbolic-cosine-type topographies, only the cases with b=100 m and 400 m are simulated as well, and they do not consider the existence of neither the reef ridge nor the lagoon (i.e., c=d=0). Table 1 presents the values of geometric parameters of various reef-face profiles adopted in all the simulations. In this table, $\bar{h}_{\mathrm{R}}$ refers to the mean water depth over the reef face, which can be formulated as:

$$\bar{h}_{\mathrm{R}}=\frac{1}{b}\int_{-200-b}^{-200}h_{\mathrm{R}}(x)dx. \tag{5}$$

Table 1. Geometric parameters of various reef-face profiles and wave parameters of the incident solitary waves used in all the simulations. A_0 denotes the incident solitary wave height.

Topography	Geometric parameters		A_0
Arc-tangent-type	b=100 m	α=2.7 m, $\bar{h}_{\mathrm{R}}$=5.42 m	0.02 m, 0.05 m, 0.10 m, 0.15 m
		α=3.3 m, $\bar{h}_{\mathrm{R}}$=4.70 m	
	b=400 m	α=2.7 m, $\bar{h}_{\mathrm{R}}$=5.42 m	
		α=3.3 m, $\bar{h}_{\mathrm{R}}$=4.70 m	
Plane	b=5, 100, 200, 300 and 400 m, S=0.80–0.01, $\bar{h}_{\mathrm{R}}$		
Hyperbolic-cosine-type	b=100 m	κ=0.15, $\bar{h}_{\mathrm{R}}$=3.51 m	
		κ=150, $\bar{h}_{\mathrm{R}}$=3.05 m	
	b=400 m	κ=0.15, $\bar{h}_{\mathrm{R}}$=3.51 m	
		κ=150, $\bar{h}_{\mathrm{R}}$=3.05 m	

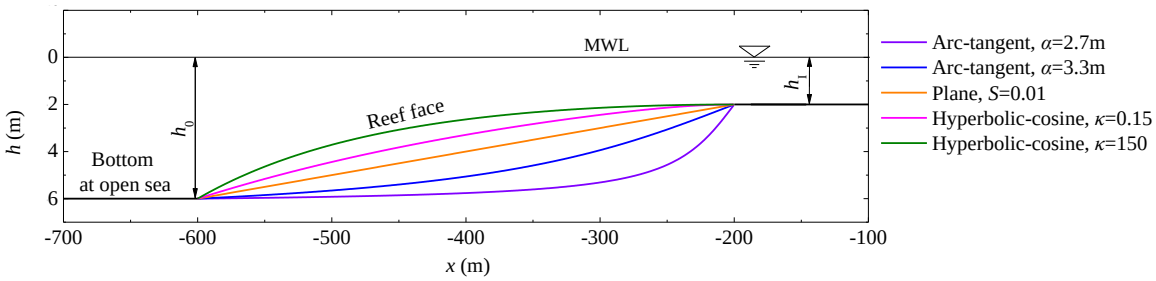

Fig. 4. Comparison of various reef-face profiles (taking the fringing reef with the reef-face width of b=400 m as an example)

To intuitively illustrate the differences of the reef-face topographies presented in Table 1, various reef-face profiles for the fringing reef with the reef-face width of b=400 m, the reef-ridge width of c=40 m and the lagoon width of d=40 m are compared in Fig. 4. For the two arc–tangent-type topographies, the variation of α results in different the mean water depths over the reef face; the values of α=2.7 m and 3.3 m obtain the mean water depths of $\bar{h}_R$ =5.42 m and 4.70 m, respectively. Analogously, for the two hyperbolic-cosine-type topographies, the mean water depths $\bar{h}_R$ are also different because of different values of κ; κ=0.15 and 150 correspond to $\bar{h}_R$ =3.51 m and 3.05 m, respectively. For the plane-slope topography, the mean water depth over the reef face is $\bar{h}_R$ =4.00 m, which falls between those of the arc-tangent-type topography with α=3.3 m and the hyperbolic-cosine-type topography with κ=0.15. For the reef face with the width of b=100 m, the various topographical profiles presented in Table 1 are identical to those illustrated in this figure except that the reef-face width is quartered.

In the current study, four different incident solitary wave heights are considered, i.e., A_0=0.02 m, 0.05 m, 0.10 m and 0.15 m (refer to Table 1). The initial incident solitary wave is expressed as (Madsen et al., 2008):

$$\eta(x) = A_0 \mathrm{sech}^2\left[k(x-x_0)\right],\ k = \sqrt{\frac{3A_0}{4h^3}}, \tag{6}$$

and the initial velocity is taken as a linear expression

$$u(x) = \sqrt{\frac{g}{h}}\eta(x), \tag{7}$$

where g, A_0, and x_0 denote the gravitational acceleration, the wave amplitude and the center position of the initial incident solitary wave, respectively. As an initial condition, in each case, the wavefront of the initial incident wave is set at the toe of the reef face (the wavefront of the incident solitary

wave is defined as $\eta_f = 0.05A_0$, where η_f denotes the free surface elevation of the wavefront).

As the numerical wave tank shown in Fig. 1 is symmetric with respect to the x-axis, in order to save the computing cost, only half of the wave tank (i.e. $y \geq 0$) is utilized as the computational domain of the numerical simulations. Throughout the numerical wave tank, the uniform grid size of Δx=Δy= 0.25 m is used, and the computational domain (i.e., $y \geq 0$) consists of 390,461 nodes and 384,000 rectangular elements. The total simulation time of 300.0 s is adopted for all cases.

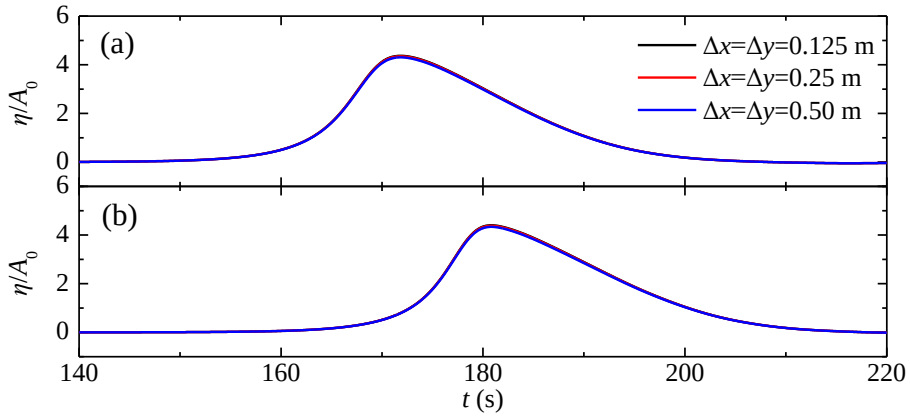

Fig. 5. Time series of the free-surface elevations at gauge G_1 excited by the incident solitary wave with A_0=0.05 m for three different grid sizes for two cases. For the case in (a), the offshore reef has the plane reef-face slope with b=400 m and without neither the reef ridge nor the lagoon (i.e., c=d=0). The reef topography at the case in (b) has the almost identical to that in (a) except that the reef face becomes the hyperbolic-cosine type with κ=150.

To examine whether the grid size of Δx=Δy=0.25 m is fine enough to gain convergent numerical results, two different grid sizes, namely, Δx=Δy=0.125 m and Δx=Δy=0.5 m, are also utilized to perform the simulations for the following two cases. In the first case, the offshore reef has a plane reef-face slope with b=400 m and without neither the reef ridge nor the lagoon (i.e., c=d=0), and the incident solitary wave has a wave height of A_0=0.05 m. The second case has the almost identical reef topography and the same incident wave height with those in the first case except that the reef face becomes the hyperbolic-cosine type with κ=150. In each case, the initial incident wave condition and the layout and size of the numerical wave tank for the three grid sizes are set to be identical. Fig. 5 presents the comparison of the time series of the free-surface elevations at gauge G_1 for the three grid sizes in both cases. It is clearly observed that the numerical results acquired by

these three grid sizes are almost identical to each other, which indicates that the grid size $\Delta x=\Delta y=0.25$ m adopted in this article can indeed gain convergent numerical results. It can also be seen that the moment at which the maximum runup occurs at the backwall of the harbor for the case shown in Fig. 5a is obviously less than that for the case shown in Fig. 5b. This is due to the fact that the mean water depth over the reef face for the former case is $\bar{h}_{\mathrm{R}}=4.00$, which is larger than that for the latter case, $\bar{h}_{\mathrm{R}}=3.05$ m (refer to Table 1). Hence, the propagation velocity of the incident solitary wave over the reef face for the former is larger than that for the latter.

4. Results and discussion

It is obvious that how the offshore reef affects the characteristics of the transient harbor resonance excited by transient long waves, such as solitary waves, is closely related to the evolution features of the incident wave height over the reef. Hence, evolutions of the incident wave height over different offshore reefs are first illustrated and discussed in Section 4.1. Subsequently, to facilitate the reader's understanding of the related contents about the wave energy distribution and the total wave energy inside the harbor, the calculation process of the response amplitudes of the different resonant modes is described in Section 4.2. Finally, the effects of the four geometrical parameters, including the plane reef-face slope, the reef-ridge width, the lagoon width and the reef-face profile shape, on the transient harbor oscillations are presented and discussed in Sections 4.3–4.6, respectively.

4.1. Wave height evolutions over the offshore reef

To comprehensively embody the evolution feature of the incident solitary wave over the reef, the wave height evolutions over four typical offshore reef topographies (i.e., Topographies I–IV) are discussed in this section. Topographies I and II correspond to those used in the two cases of Fig. 5a and b, respectively. Both Topographies III and IV have the almost identical reef profile shape with Topography I except that a reef ridge with c=40 m and a lagoon with d=80 m are considered in Topographies III and IV, respectively.

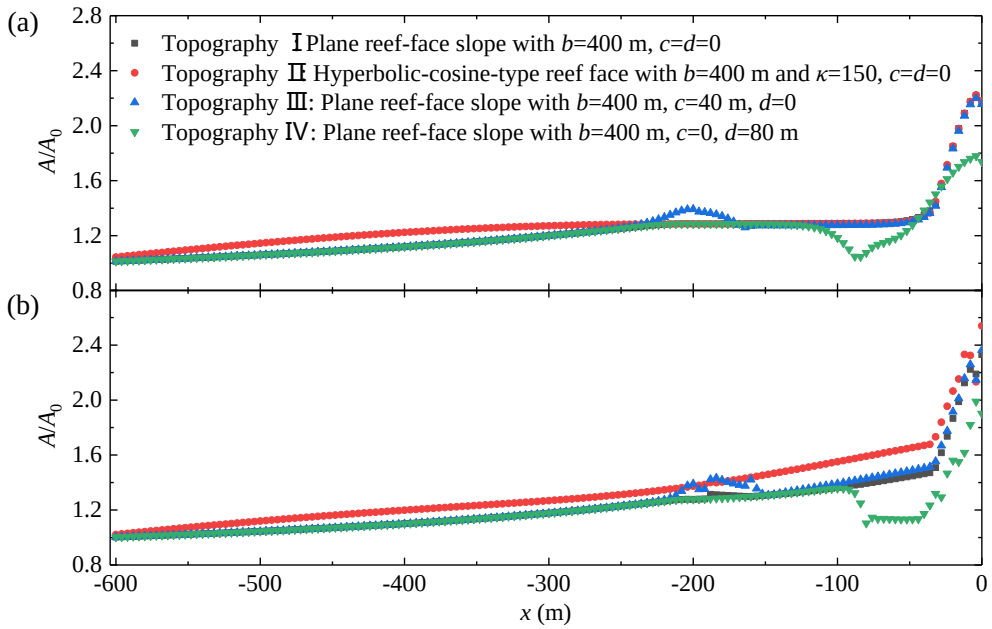

Fig. 6. Wave height evolutions of the incident solitary waves with (a) A_0=0.05 m and (b) A_0=0.15 m over four different offshore reef topographies (i.e., Topographies I–IV). The topographies I and II in this figure correspond to those used in the two cases of Fig. 5a and b, respectively.

Fig. 6 demonstrates the wave height evolutions of the incident solitary waves with A_0=0.05 m and A_0=0.15 m over the four typical offshore reef topographies. When the wave height of the incident wave height is relatively small (i.e., A_0=0.05 m), three obvious phenomena can be easily seen (see Fig. 6a). Firstly, at the range of the reef face (i.e., –600 m ≤ x < –200 m), because Topographies I, III and IV have the identical plane reef face, the wave height evolutions of the solitary waves over the reef face for these three topographies are also almost identical with each other. While for Topography II, the solitary wave heights over the most area of the reef face are obviously larger than those for the other three topographies, which is attributed to the smaller local water depth over the reef face for Topography II compared to that for the other three topographies (refer to Fig. 4). Secondly, at the range of –200 m ≤ x < –100 m, because there is no reef ridge for Topographies I, II and IV, the wave height evolutions for them are very similar; while because of the existence of the reef ridge for Topographies III, the solitary wave heights near the reef edge at x=–200 m for this topography become notably larger than those for the other three topographies. Thirdly, at the range of –100 m ≤ x < 0, the wave height evolutions for Topographies I–III are very similar due to that no lagoon is arranged for these topographies; while for Topography IV, the wave

heights are significantly less than those for the other three topographies inside the lagoon and near the harbor entrance at x=0, which is caused by the significant increase of the water depth inside the lagoon.

When the wave height of the incident wave height is relatively large (i.e., A_0=0.15 m), two different phenomena can be clearly observed comparing with those with A_0=0.05 m. Firstly, at the range of the whole offshore reef (i.e., –600 m ≤ x < 0), the solitary wave heights for Topography II are almost completely larger than those for Topographies I, III and IV over the whole range of the offshore reef except near the reef ridge for Topography III. Secondly, at the range of –100 m ≤ x < 0, the wave heights for Topography IV become notably lower than those for the other three topographies at the whole range, rather other just inside the lagoon and near the harbor entrance. In addition, the wave height evolutions for Topographies I–III are shown to have obvious differences although there is no lagoon arranged for all these three topographies. Overall, the wave heights for Topography III are slightly greater than those for Topography I, and both of them becomes significantly lower than those for Topography II.

4.2. Calculation process of the response amplitudes of the different resonant modes

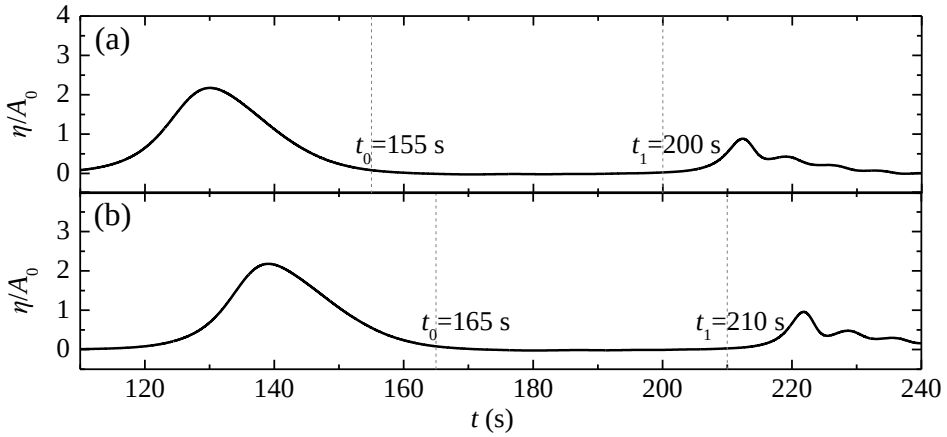

Fig. 7. Time histories of the free surface elevations at gauge G_{51} for the two cases shown in Fig. 5. The cases in (a) and (b) correspond to those in Fig. 5a and b, respectively.

In all simulations, only the wave field data during the period from t_0 to t_1 are utilized to separate the response amplitudes of different resonant modes inside the harbor. The parameters t_0 and t_1 respectively refer to the moment that the incident solitary wave from the open sea completely enters

the harbor and the moment that the reflected wave from the backwall of the harbor at x=200 m begins to propagate out of the harbor. Taking the two cases shown in Fig. 5 for example, Fig. 7 presents the time histories of the free surface elevations at gauge G_{51} placed at the harbor entrance in both cases. For the case in Fig. 5a, the incident solitary wave has already totally entered the harbor at t_0=155 s, and the reflected wave from the backwall begin to propagate out of the harbor at t_1=200 s (see Fig. 7a). While for the case in Fig. 5b, because the mean water depth over the reef face is less than that for the former case, the moments t_0 and t_1 increase up to 165 s and 210 s, respectively.

Fig. 8 presents the comparisons of the simulated free surfaces utilizing FUNWAVE-TVD and the corresponding fitted free surfaces by the NMD method for the two cases in Fig. 5. The lowest forty resonant modes are used to fit the simulated free surface in the NMD method. For both cases, the fitted free surfaces are shown to agree very well with the simulated free surfaces. For the first case (Fig. 8a), the simulated free surface has a maximum runup of 0.2174 m at the back wall of the harbor (i.e., at x=200 m) and t=171.8 s; at the same position and the same time, the fitted free surface has a maximum runup of 0.2142 m. For the second case (Fig. 8b), the simulated free surface has a maximum runup of 0.2190 m at x=200 m and t=180.7 s; at the same position and the same time, the fitted free surface has a maximum runup of 0.2155 m. Due to the significance and typicality of the maximum runup inside the harbor, we define the numerical fitting error (*NFE*) of the NMD method to be the relative error between the simulated and the fitted maximum runups, that is,

$$NFE = \left| \frac{A_{\mathrm{m}} - (A_{\mathrm{m}})_{\mathrm{fitted}}}{A_{\mathrm{m}}} \right| \times 100\% , \tag{8}$$

where A_{m} and $(A_{\mathrm{m}})_{\mathrm{fitted}}$ refer to the simulated and the fitted maximum runups, respectively. The *NFE* embodies the accuracy of the NMD method in decomposing the response amplitudes of different resonant modes. The *NFE*s for the two cases shown in Fig. 8a and b are 1.47% and 1.60%, respectively. Once the response amplitudes of different modes are obtained, the total wave energy inside the harbor can be calculated accurately as follows (Gao et al., 2016b):

$$E = \sum_{i=1}^{40} \frac{1}{2} A_i^2 , \tag{9}$$

where A_i (i=1, 2,…, 40) refers to the response amplitude of the i-th resonant mode.

(a)

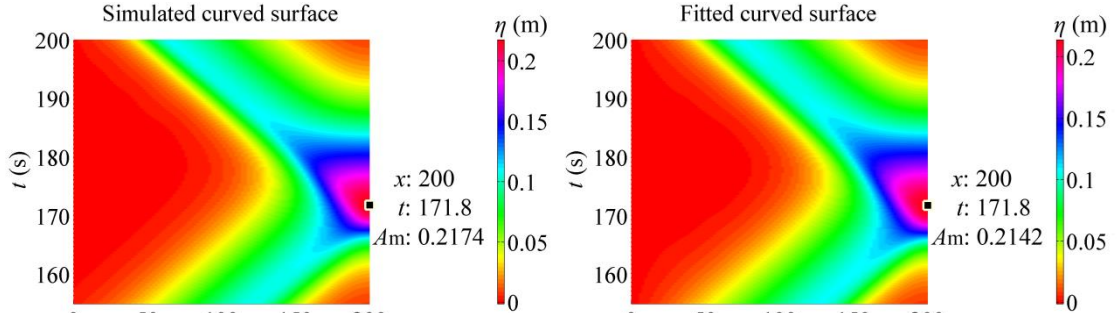

Fig. 8. Comparison of the simulated free surfaces and the corresponding fitted free surfaces for the two cases shown in Fig. 5. The cases in (a) and (b) correspond to those in Fig. 5a and b, respectively.

Through calculating the *NFE*s for all the simulations in this article (the specific results are not shown here), it is found that the *NFE*s for all the cases with the incident wave height $A_0 \leq 0.10$ m are less than 5.0%, which guarantees the accurate prediction of the response amplitudes of the different resonant modes. For all the simulations with A_0=0.15 m, however, the *NFE*s in most of these cases exceed 5.0%, which means that the accurate prediction of the response amplitudes of the different resonant modes cannot be ensured for these cases with the largest incident wave height. Hence, in the following sections, the related results and discussion about the wave energy distributions and the total wave energy inside the harbor are only restricted to the cases with $A_0 \leq 0.10$ m.

4.3. Effect of the reef-face slope on transient harbor oscillations

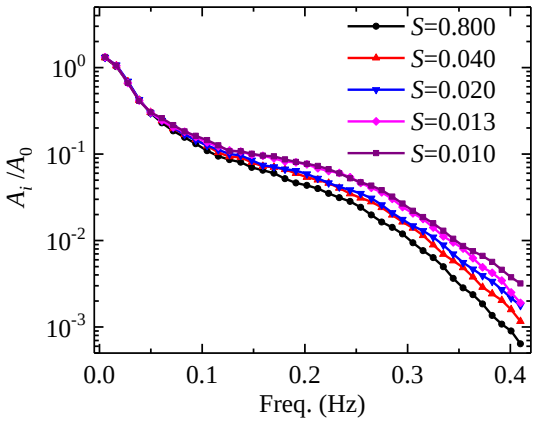

Fig. 9. Response amplitudes of the lowest forty resonant modes inside the harbor excited by the incident solitary wave with A_0=0.10 m for the reef topographies with various plane reef-face slopes.

This section investigates the effects of the plane reef-face slope on transient harbor oscillations. Hence, only the offshore reef topographies with various plane reef-face slopes (5 m $\leq b \leq$ 400 m, or equivalently, $0.8 \geq S \geq 0.01$) and without neither the reef ridge nor the lagoon are considered here. Fig. 9 presents the decomposed response amplitudes of the lowest forty resonant modes inside the harbor excited by the incident solitary wave with A_0=0.10 m for the reef topographies with various plane reef-face slopes. For the lowest five resonant modes, it is clear that the response amplitudes of each mode for all the reef-face slopes considered in this paper are almost identical. However, for the higher modes, it is shown that the larger reef-face slope always results in the smaller response amplitudes of these modes. Therefore, as a whole, when the reef-face slope is large, the wave energy inside the harbor is mainly concentrated in the lowest few resonant modes, and only a very small proportion of the wave energy is distributed over the higher modes. As the reef-face slope decreases, the proportion of the wave energy possessed by the higher modes increases gradually, and the distribution of the wave energy inside the harbor over the various modes tends to become more uniform.

In order to better compare the uniformity of the wave energy distribution inside the harbor under various incident wave heights and various offshore reef topographies, it is necessary to further quantify the uniformity of the wave energy distribution. Identical to Gao et al. (2017a), the coefficients of variance (*CV*) of the response amplitudes of the lowest forty resonant modes for all cases are calculated as follows:

$$CV = \frac{\sigma}{\mu}, \tag{10}$$

where

$$\sigma = \sqrt{\frac{1}{40}\sum_{i=1}^{40}(A_i - \mu)^2}, \tag{11}$$

$$\mu = \frac{1}{40}\sum_{i=1}^{40} A_i . \tag{12}$$

The *CV* value can embody the discrete degree of the response amplitude of different modes relative to their average value more intuitively. Apparently, the smaller the *CV* value is, the more uniform the wave energy distribution inside the harbor over different resonant modes is.

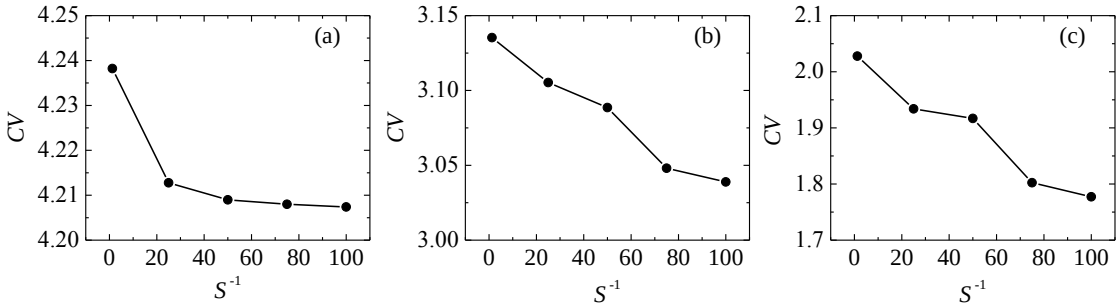

Fig. 10. Variations of the *CV* values of the wave amplitude distributions inside the harbor with respect to the slope coefficient, S^{-1}, under the conditions of (a) A_0=0.02 m, (b) A_0=0.05 m and (c) A_0=0.10 m.

Fig. 10 presents the variations of the *CV* values of the wave amplitude distributions inside the harbor with respect to the plane slope coefficient, S^{-1}, under the conditions of A_0=0.02 m, 0.05 m and 0.10 m. Two obvious phenomena can be easily observed. Firstly, for all the three incident wave heights, the *CV* value decreases monotonically with the decrease of the plane reef-face slope, which is consistent with the qualitative findings for Fig. 9. Secondly, via comparing the variation ranges of the *CV* values presented in Fig. 10a, b and c, the *CV* values for A_0=0.05 m are always lower than those for A_0=0.02 m, and meanwhile, always larger than those for A_0=0.10 m. This indicates that the larger incident solitary wave height always results in the more uniform distribution of the wave energy over various resonant modes inside the harbor. This phenomenon coincides with the related finding in Gao et al. (2016b).

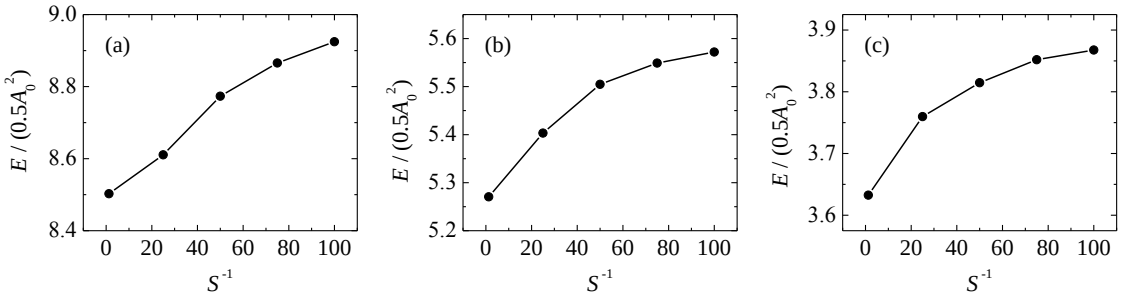

Fig. 11. Variations of the non-dimensional total wave energy inside the harbor, $E/(0.5A_0^2)$, with respect to the slope coefficient, S^{-1}, under the conditions of (a) A_0=0.02 m, (b) A_0=0.05 m and (c) A_0=0.10 m.

As mentioned in Section 4.2, the total wave energy inside the harbor can be accurately calculated by the formula, Eq. (9). Fig. 11 demonstrates the variations of the non-dimensional total wave energy inside the harbor, $E/(0.5A_0^2)$, with respect to the slope coefficient, S^{-1}, under the conditions of A_0=0.02 m, A_0=0.05 m and A_0=0.10 m. It is clear that for all the three incident wave heights, the total wave energy inside the harbor gradually decreases with the increase of the reef-face slope. It indicates that the energy reflections of the incident solitary waves over the plane reef face gradually increase with the increase of the reef-face slope when the incident solitary waves propagate from the open sea to the harbor.

From the viewpoint of tsunami-induced coastal flooding, the maximum wave runup inside the harbor, A_m, is directly related to the submersion near the port zone. Hence, it is essential to further examine how the plane reef-face slope affects the maximum wave runup inside the harbor, A_m. Fig. 12 presents the variations of the amplification factors of the incident solitary waves inside the harbor, A_m/A_0, with respect to the slope coefficient, S^{-1}, under various incident wave heights. Three obvious phenomena can be easily observed. Firstly, for all the incident wave heights considered in this paper, the amplification factors of the incident solitary waves inside the harbor, A_m/A_0, decrease gradually with the increase of the reef-face slope. This phenomenon coincides with the finding shown in Fig. 11, and is also attributed to the increasing reflected wave energy over the plane reef face as the reef-face slope increases. Secondly, the sensitivity of the amplification factor, A_m/A_0, to the reef-face slope closely depends on the incident solitary wave height. Specifically, as the reef-face slope increases, the decrements of A_m/A_0 for the smaller incident wave heights (i.e., A_0=0.02 m and 0.05

m) are obviously less than those for the larger incident wave heights (i.e., A_0=0.10 m and 0.15 m). At the variation range of the reef-face slope considered in this paper, the decrements of A_m/A_0 for A_0=0.02 m, 0.05 m, 0.10 m and 0.15 m are 0.121, 0.057, 0.719 and 0.760, respectively. Thirdly, for each reef topography with the plane reef face, the amplification factor, A_m/A_0, is always shown to slightly decrease first and then sharply increase as the incident solitary wave height increases from A_0=0.02 m to 0.15 m.

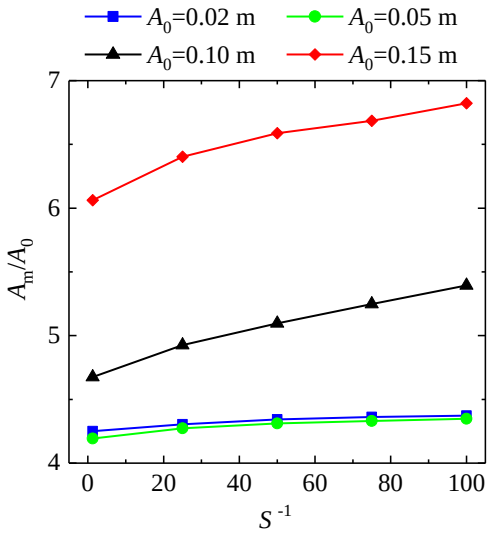

Fig. 12. Variations of the amplification factors of the incident solitary waves inside the harbor, A_m/A_0, with respect to the slope coefficient, S^{-1}, under various incident wave heights.

4.4. Effect of the reef-ridge width on transient harbor oscillations

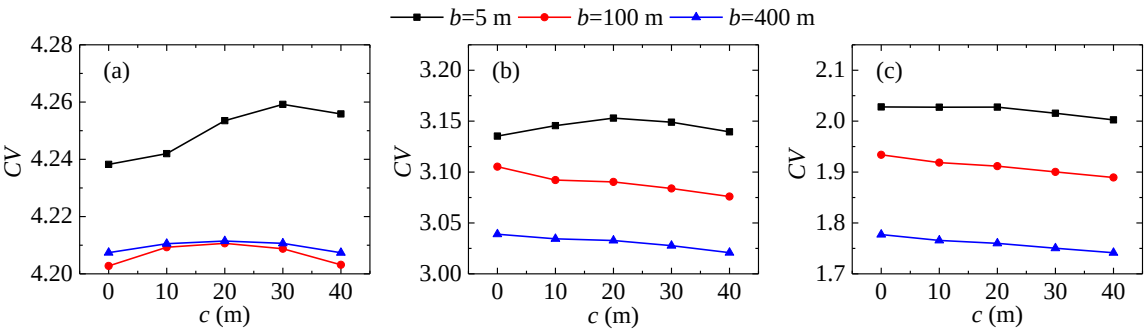

Fig. 13. Variations of the *CV* values of the wave amplitude distributions inside the harbor with respect to the reef-ridge width, *c*, under the conditions of (a) A_0=0.02 m, (b) A_0=0.05 m and (c) A_0=0.10 m.

This section studies the influences of the reef-ridge width on transient harbor resonance. Therefore, only the offshore reef topographies with various reef-ridge widths ($0 \le c \le 40$ m) and the three plane reef-face widths (b=5 m, 100 m and 400 m) and without the lagoon are considered here. Fig. 13 illustrates the variations of the *CV* values of the wave amplitude distributions inside the harbor with respect to the reef-ridge width, c, under the conditions of A_0=0.02 m, 0.05 m and A_0=0.10 m. It is seen that the changing trend of the *CV* value with respect to the reef-ridge width, c, depends on both the incident wave height, A_0, and the reef-face width, b. When the incident solitary wave has the smallest wave height, i.e., A_0=0.02 m (see Fig. 13a), the *CV* value is shown to increase first and then decrease with the increase of the reef-ridge width, c, regardless of the reef-face width, b. When the incident solitary wave height rises to A_0=0.05 m (see Fig. 13b), the offshore reef topographies with different reef-face widths presents different changing trends of the *CV* value with respect to the reef-ridge width. For the offshore reef with b=5 m, the trend of the *CV* value is similar to those shown in Fig. 13a; while for the reefs with b=100 m and 400 m, the *CV* values are shown to monotonically decrease with the reef-ridge width. When the incident solitary wave height increases further to A_0=0.10 m (see Fig. 13c), for all the three reef-face widths considered, the *CV* values always monotonically decrease with the reef-ridge width, c. Hence, it can be concluded that for the combination of smaller incident wave height and smaller reef-face width, the uniformity of the wave energy distribution inside the harbor tends to first decrease and then increase with the reef-ridge width; while for the combination of larger incident wave height and larger reef-face width, the uniformity of the wave energy distribution inside the harbor tends to gradually increase with the reef-ridge width.

Fig. 14 shows the variations of the non-dimensional total wave energy inside the harbor, $E/(0.5A_0^2)$, with respect to the reef-ridge width, c, under the conditions of A_0=0.02 m, 0.05 m and A_0=0.10 m. It can be clearly observed that the total wave energy inside the harbor, E, always monotonically decreases with the increase of the reef-ridge width, c, regardless of the incident solitary wave height, A_0, and the reef-face width, b. This is due to the fact that the larger dimensions of the reef ridge tend to cause the larger reflected wave energy as the incident solitary wave propagates through the reef ridge.

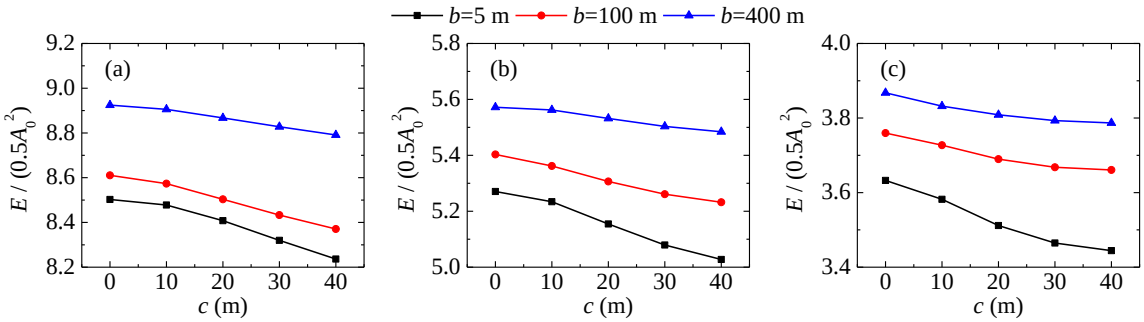

Fig. 14. Variations of the non-dimensional total wave energy inside the harbor, $E/(0.5A_0^2)$, with respect to the reef-ridge width, c, under the conditions of (a) A_0=0.02 m, (b) A_0=0.05 m and (c) A_0=0.10 m.

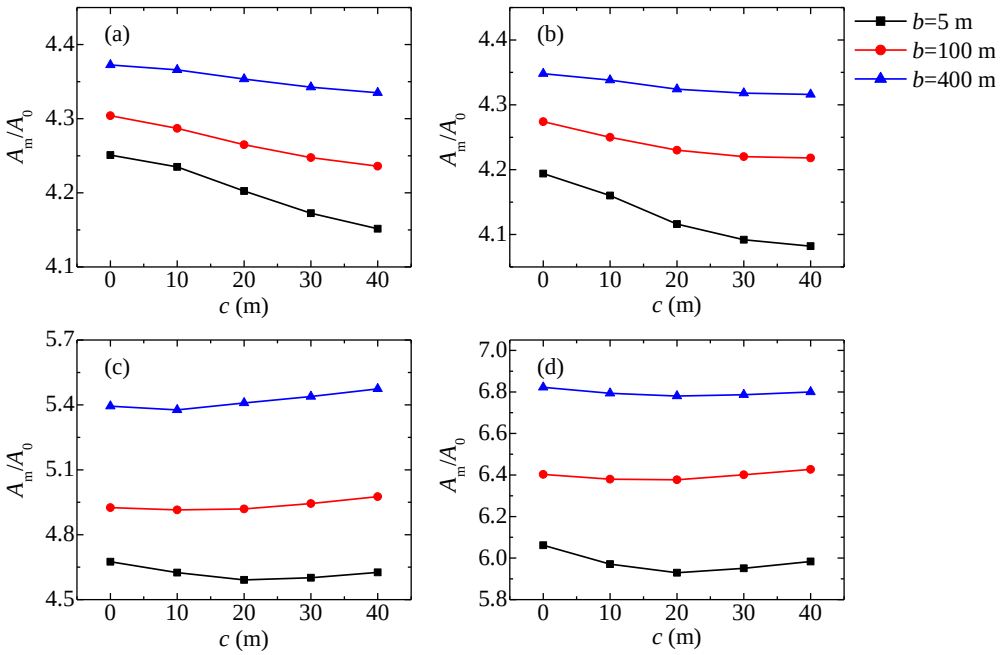

Fig. 15. Variations of the amplification factors of the incident solitary waves, A_m/A_0, inside the harbor with respect to the reef-ridge width, c, under the conditions of (a) A_0=0.02 m, (b) A_0=0.05 m, (c) A_0=0.10 m and (d) A_0=0.15 m.

Fig. 15 presents the variations of the amplification factors of the incident solitary waves inside the harbor, A_m/A_0, with respect to the reef-ridge width, c, under various incident wave heights. It is clear that the changing trend of A_m/A_0 with respect to the reef-ridge width depends closely on the incident solitary wave height. For the relatively smaller incident solitary wave heights, i.e., A_0=0.02 m and 0.05 m (see Fig. 15a and b), the amplification factors, A_m/A_0, decrease gradually with the

increase of the reef-ridge width. The phenomenon coincides with the decreasing tendency of the total wave energy inside the harbor with the reef-ridge width revealed in Fig. 14, and it is also attributed to the fact that the larger dimensions of the reef ridge tend to cause the larger reflected wave energy. However, for the relatively larger incident solitary wave heights, i.e., A_0=0.10 m and 0.15 m (see Fig. 15c and d), the amplification factor, A_m/A_0, does not decline gradually with the reef-ridge width any more, and it exhibits decrease first and then increase with the latter. The specific reason for this phenomenon will be elaborated in the following paragraph.

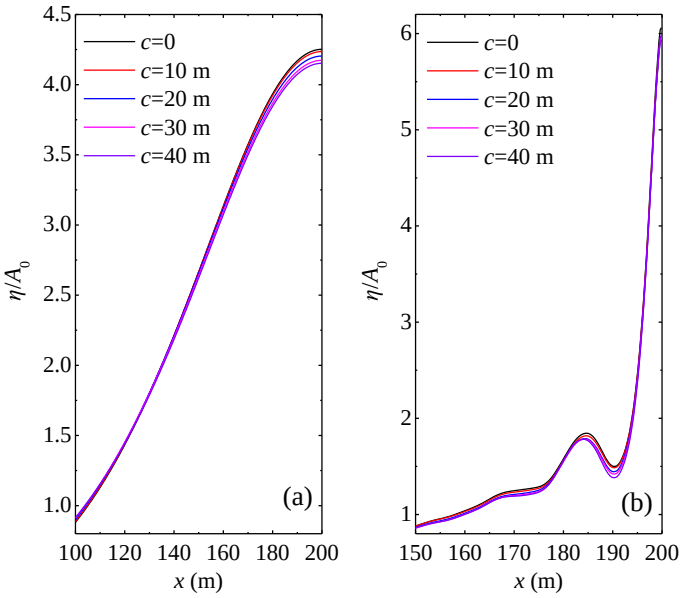

Fig. 16. Wave profiles along the center line of the harbor at the moments that the maximum runups on the backwall of the harbor (at x=200 m) occur for (a) A_0=0.02 m and (b) A_0=0.15 m under the conditions of various reef-ridge widths and b=5 m.

In order to further explain why the variation tendency of the amplification factor, A_m/A_0, with the reef-ridge width coincides with that of the total wave energy inside the harbor when the incident solitary wave height is relatively small and why this consistency does not exist for relatively larger incident wave heights anymore, Fig. 16 demonstrates the wave profiles along the center line of the harbor at the moments that the maximum runups on the backwall of the harbor (at x=200 m) occur for A_0=0.02 m and A_0=0.15 m under the conditions of various reef-ridge widths and b=5 m. When the incident solitary wave has the smallest wave height, i.e., A_0=0.02 m (see Fig. 16a), each of the wave profiles under various reef-ridge widths only has a maximum wave crest located at the

backwall of the harbor. In other words, the overwhelming majority of the wave energy is only concentrated at the backwall. Under this condition, the larger total wave energy inside the harbor inevitably results in the larger amplification factor of the incident solitary wave, A_m/A_0. On the contrary, when the incident solitary wave has the largest wave height, i.e., A_0=0.15 m (see Fig. 16b), for all the reef-ridge widths considered in this article, besides the maximum wave crests located at the backwall of the harbor, there are obvious secondary crests approximately at x=185 m. In addition, it can be found that the larger the total wave energy inside the harbor is, the higher the secondary crest becomes. Because there is significant wave energy scattered in the secondary crest, under this case, the larger total wave energy inside the harbor does not necessarily lead to the larger amplification factor of the incident solitary wave, A_m/A_0.

4.5. Effect of the lagoon width on transient harbor oscillations

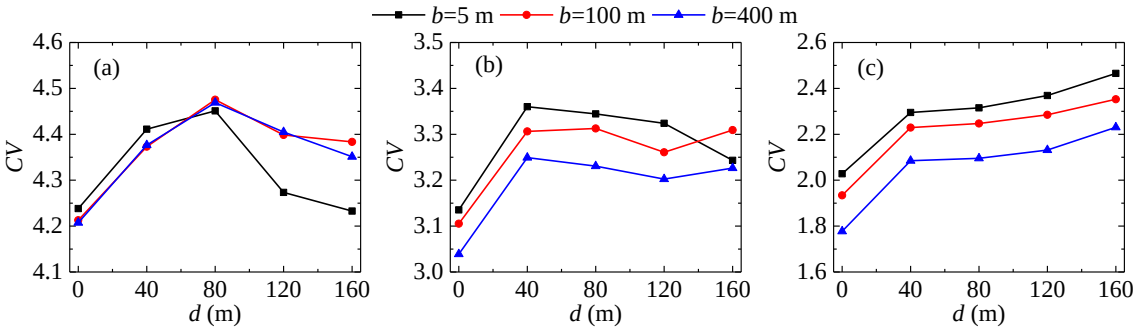

Fig. 17. Variations of the *CV* values of the wave amplitude distributions inside the harbor with respect to the lagoon width, d, under the conditions of (a) A_0=0.02 m, (b) A_0=0.05 m and (c) A_0=0.10 m.

This section discusses the effects of the lagoon width on transient harbor resonance. Hence, only the offshore reef topographies with various lagoon widths ($0 \le d \le 160$ m) and the three plane reef-face widths (b=5 m, 100 m and 400 m) and without the reef ridge are considered here. Fig. 17 demonstrates the variations of the *CV* values of the wave amplitude distributions inside the harbor with respect to the lagoon width, d, under the conditions of A_0=0.02 m, 0.05 m and A_0=0.10 m. It is clear that the changing trend of the *CV* value with respect to the lagoon width, d, depends on both the incident wave height, A_0, and the reef-face width, b. When the incident solitary wave has the smallest wave height, i.e., A_0=0.02 m (see Fig. 17a), the *CV* value increases first and then decreases with the increase of the lagoon width, d, regardless of the reef-face width, b. When the incident

solitary wave height increases to A_0=0.05 m (see Fig. 17b), the offshore reef topographies with different reef-face widths shows different changing trends of the *CV* value with respect to the lagoon width. For the reef with *b*=5 m, the trend of the *CV* value is similar to those shown in Fig. 17a; while for the reefs with *b*=100 m and 400 m, the *CV* values are shown to first increase, then decrease and then increase with the increase of the lagoon width. When the incident solitary wave height further rises to A_0=0.10 m (see Fig. 17c), for all the three reef-face widths considered, the *CV* values are always shown to increase monotonically with the lagoon width. Therefore, based on the above observations, it can be concluded that for the combination of smaller incident wave height and smaller reef-face width, the uniformity of the wave energy distribution inside the harbor tends to first decrease and then increase with the lagoon width; while for the combination of larger incident wave height and larger reef-face width, the uniformity of the wave energy distribution inside the harbor tends to gradually decrease with the reef-ridge width.

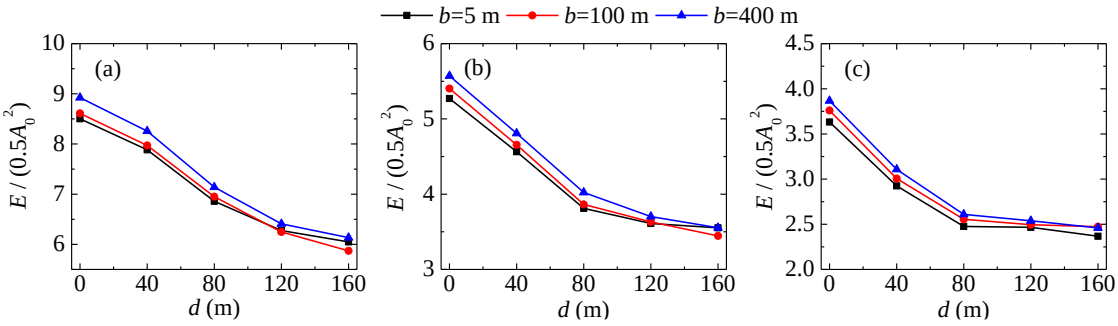

Fig. 18. Variations of the non-dimensional total wave energy inside the harbor, $E/(0.5A_0^2)$, with respect to the lagoon width, *d*, under the conditions of (a) A_0=0.02 m, (b) A_0=0.05 m and (c) A_0=0.10 m.

Fig. 18 shows the variations of the non-dimensional total wave energy inside the harbor, $E/(0.5A_0^2)$, with respect to the lagoon width, *d*, under the conditions of A_0=0.02 m, 0.05 m and A_0=0.10 m. Two obvious phenomena can be easily observed. Firstly, similar to the phenomenon in Fig. 14, the total wave energy inside the harbor, *E*, is always shown to monotonically decrease with the increase of the lagoon width, *d*, regardless of the incident solitary wave height, A_0, and the reef-face width, *b*. This is because the lagoon can cause part of the incident wave energy to be reflected towards the open sea and also cause part of the incident wave energy to be trapped inside the lagoon.

In addition, the larger the lagoon size is, the larger the incident wave energy loss (including the reflected wave energy towards the open sea and the trapped wave energy inside the lagoon) becomes. Secondly, for all the three incident wave heights and all the three reef-face widths considered, in general, the decreasing rates of the total wave energy inside the harbor always present decreasing trends as the lagoon width increases. Hence, it can be inferred that although the larger the lagoon size can lead to the larger the incident wave energy loss owing to the lagoon, the increasing rate of the latter tends to decrease with the increase of the former.

Fig. 19 presents the variations of the amplification factors of the incident solitary waves inside the harbor, A_m/A_0, with respect to the lagoon width, d, under various incident wave heights. Similar to the two phenomena shown in Fig. 18, the amplification factor, A_m/A_0, is also shown to gradually decrease with the lagoon width, d, regardless of the incident solitary wave height, A_0, and the reef-face width, b. Besides, overall, the decreasing rates of the amplification factor, A_m/A_0, always present decreasing trends with the increase of the lagoon width for all the incident wave heights and all the reef-face widths considered.

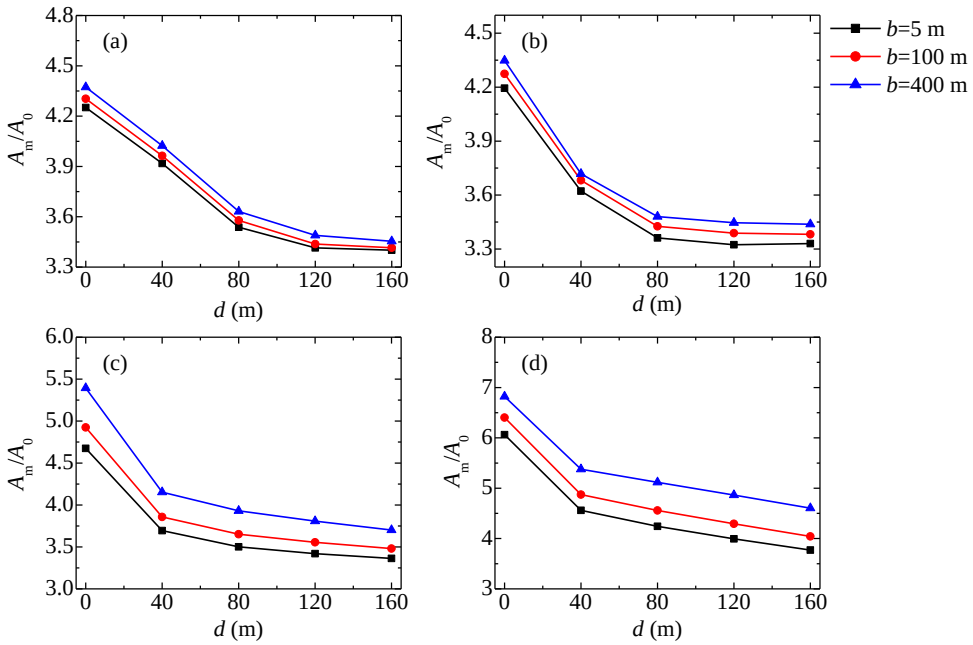

Fig. 19. Variations of the amplification factors of the incident solitary waves, A_m/A_0, inside the harbor with respect to the lagoon width, d, under the conditions of (a) A_0=0.02 m, (b) A_0=0.05 m, (c) A_0=0.10 m and (d) A_0=0.15 m.

4.6. Effect of the reef-face profile shape on transient harbor oscillations

This section investigates the influences of the reef-face profile shape on transient harbor oscillations. Therefore, only the offshore reef topographies with various reef-face profile shapes (3.05 m $\leq \bar{h} \leq$ 5.42 m) and the two plane reef-face widths (b=100 m and 400 m) and without neither the reef ridge nor the lagoon are considered here. Fig. 20 illustrates the variations of the *CV* values of the wave amplitude distributions inside the harbor with respect to the mean water depth over the reef face, $\bar{h}_R$, under the conditions of A_0=0.02 m, 0.05 m and A_0=0.10 m. It is clearly seen that for all the three incident wave heights and both the reef-face widths considered, the *CV* values are always shown to gradually increase with the mean water depth over the reef face, $\bar{h}_R$. This indicates that the uniformity of the wave energy distribution inside the harbor tends to gradually decrease as the mean water depth over the reef face, $\bar{h}_R$, increases.

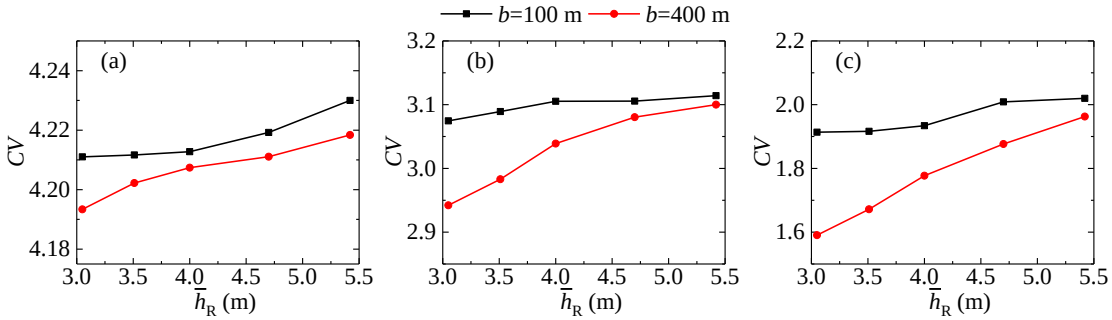

Fig. 20. Variations of the *CV* values of the wave amplitude distributions inside the harbor with respect to the mean water depth over the reef face, $\bar{h}_R$, under the conditions of (a) A_0=0.02 m, (b) A_0=0.05 m and (c) A_0=0.10 m.

Fig. 21 presents the variations of the non-dimensional total wave energy inside the harbor, $E/(0.5A_0^2)$, with respect to the mean water depth over the reef face, $\bar{h}_R$, under the conditions of A_0=0.02 m, 0.05 m and A_0=0.10 m. For all the three incident wave heights and both the reef-face widths considered, the total wave energy inside the harbor, E, is always shown to increase first and then decrease with the mean water depth over the reef face, $\bar{h}_R$. Therefore, it can be inferred that as the incident solitary wave propagates through the offshore reef, the reflected wave energy over the reef face decreases first and then increase with the mean water depth over the reef face, $\bar{h}_R$.

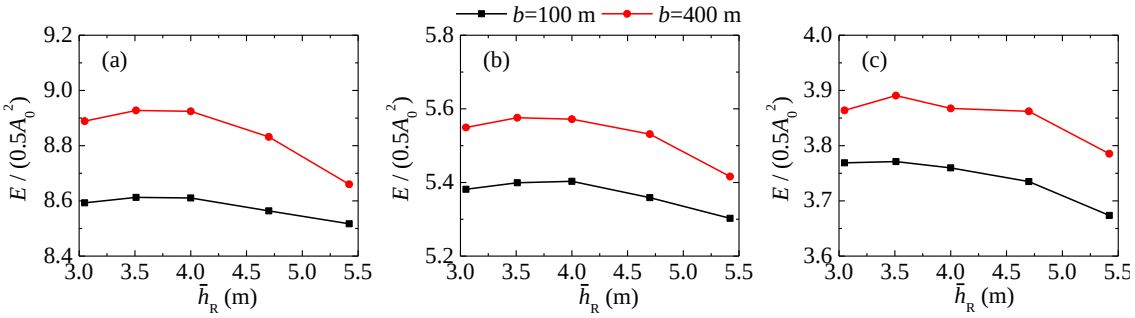

Fig. 21. Variations of the non-dimensional total wave energy inside the harbor, $E/(0.5A_0^2)$, with respect to the mean water depth over the reef face, $\bar{h}_R$, under the conditions of (a) A_0=0.02 m, (b) A_0=0.05 m and (c) A_0=0.10 m.

Fig. 22 shows the variations of the amplification factors of the incident solitary waves inside the harbor, A_m/A_0, with respect to the mean water depth over the reef face, $\bar{h}_R$, under various incident wave heights. It can easily observed that the changing trend of the amplification factor, A_m/A_0, with respect to the mean water depth, $\bar{h}_R$, is closely related to both the incident wave height, A_0, and the reef-face width, b. When the incident solitary wave has the smallest wave height, i.e., A_0=0.02 m (see Fig. 22a), the values of A_m/A_0 are shown to increase first and then decrease with the increase of the mean water depth, $\bar{h}_R$, for both the two reef-face widths considered. When the incident solitary wave height rises to A_0=0.05 m (see Fig. 22b), the reef topographies with different reef-face widths results in different changing trends of A_m/A_0 with respect to the mean water depth, $\bar{h}_R$. For the reef with b=100 m, the changing trend of A_m/A_0 is similar to those shown in Fig. 22a; while for the reef with b=400 m, the amplification factor, A_m/A_0, is shown to monotonically decrease with the increase of the mean water depth, $\bar{h}_R$. When the incident solitary wave height further rises to A_0=0.10 m and 0.15 m (see Fig. 22c and d), for both the reef-face widths considered, the amplification factors, A_m/A_0, are also shown to monotonically decrease with the increase of the mean water depth, $\bar{h}_R$. Hence, based on the above observations, it can be concluded that for the combination of smaller incident wave height and smaller reef-face width, the amplification factor of the incident solitary wave inside the harbor tends to first increase and then decrease with the mean water depth over the reef face; while for the combination of larger incident wave height and larger reef-face width, the amplification factor of the incident solitary wave inside the harbor tends to gradually decrease with the mean water depth over the reef face.

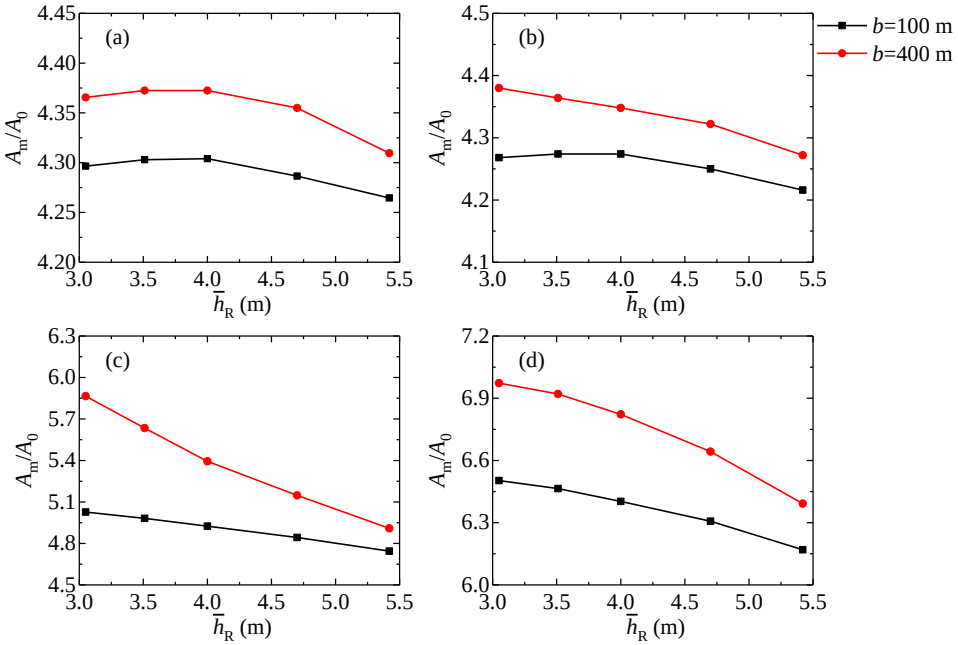

Fig. 22. Variations of the amplification factors of the incident solitary waves, A_m/A_0, inside the harbor with respect to the mean water depth over the reef face, $\overline{h}_R$, under the conditions of (a) A_0=0.02 m, (b) A_0=0.05 m, (c) A_0=0.10 m and (d) A_0=0.15 m.

5. Conclusions

Transient oscillations inside an elongated rectangular harbor excited by normal-incident solitary waves with various wave heights are simulated by utilizing the FUNWAVE-TVD model. The effects of various offshore reef topographical parameters on the wave energy distribution, the total wave energy and the maximum oscillations (runups) inside the harbor during the transient oscillations are systematically investigated for the first time in this paper. The offshore reef topographical parameters considered here include the plane reef-face slope, the reef-ridge width, the lagoon width and the variation of the reef-face profile shape. The results of this study will improve the understanding of transient harbor oscillations induced by tsunamis.

In the order of the four topographical parameters mentioned above, the following four conclusions can be drawn from the results of the present study:

1. At the variation ranges of the incident solitary wave heights and the plane reef-faces slopes, all of the uniformity of the wave energy distribution among various resonant modes, the total wave energy and the amplification factor of the incident solitary wave inside the harbor are shown to gradually decrease with the increase of the plane reef-face slope.
2. The changing trend of the uniformity of the wave energy distribution inside the harbor with

respect to the reef-ridge width depends on both the incident wave height and the reef-face width. For the combination of smaller incident wave height and smaller reef-face width, the former tends to first decrease and then increase with the latter; while for the combination of larger incident wave height and larger reef-face width, the former tends to gradually decrease with the latter. The total wave energy inside the harbor is shown to monotonically decrease with the reef-ridge width, regardless of the incident solitary wave height and the reef-face width. The changing trend of the amplification factor of the incident solitary wave inside the harbor with respect to the reef-ridge width depends closely on the incident wave height. The smaller incident wave height tends to cause the monotonic reduction of the amplification factor with the increase of the reef-ridge width, while for the larger incident wave height, the amplification factor exhibits decrease first and then increase with the reef-ridge width.

3. The changing trend of the uniformity of the wave energy distribution inside the harbor with respect to the lagoon width depends on both the incident wave height and the reef-face width. For the combination of smaller incident wave height and smaller reef-face width, the former tends to first decrease and then increase with the latter; while for the combination of larger incident wave height and larger reef-face width, the former tends to gradually decrease with the latter. Both the total wave energy and the amplification factor of the incident solitary wave inside the harbor are shown to monotonically decrease with the lagoon width, regardless of the incident solitary wave height and the reef-face width.
4. The uniformity of the wave energy distribution inside the harbor tends to gradually decrease as the mean water depth over the reef face increases. The total wave energy inside the harbor is always shown to increase first and then decrease with the mean water depth over the reef face. The changing trend of the amplification factor of the incident solitary wave inside the harbor with respect to the mean water depth, $\bar{h}_R$, is closely related to both the incident wave height and the reef-face width. For the combination of smaller incident wave height and smaller reef-face width, the former tends to first increase and then decrease with the latter; while for the combination of larger incident wave height and larger reef-face width, the former tends to gradually decrease with the latter.

Finally, we reaffirm here that these conclusions are only valid for the given harbor and the

variation ranges of the incident solitary wave height, the reef-face slope, the reef-ridge width, the lagoon width and the reef-face profile shape studied in this paper. Wave breaking over fringing reefs may remarkably change the strength and distribution of the wave energy over the reef and inside the harbor, and the further investigations which consider the effect of wave breaking will be performed in the near future.

Acknowledgments

This research is financially supported by the National Key Research and Development Program (2017YFC1404200), the National Natural Science Foundation of China (Grant Nos. 51911530205, 51609108 and 51679113), the Royal Society of UK (Grant No. IEC\NSFC\181321), the Jiangsu Government Scholarship for Overseas Studies (awarded to Dr. Junliang Gao for study abroad at the University of Bath), the Natural Science Foundation of Jiangsu Province of China (Grant No. BK20170576) and the Natural Science Research of Jiangsu Higher Education Institutions of China (Grant No. 17KJB580006).

References

Bellotti, G., Briganti, R., Beltrami, G.M., 2012. The combined role of bay and shelf modes in tsunamis amplification along the coast. Journal of Geophysical Research: Oceans 117, C08027, doi: 10.1029/2012JC008061.

Booij, N., 1983. A note on the accuracy of the mild-slope equation. Coastal Engineering 7 (3), 191-203.

Chen, Q., 2006. Fully nonlinear Boussinesq-type equations for waves and currents over porous beds. Journal of Engineering Mechanics 132 (2), 220-230.

De Jong, M.P.C., Battjes, J.A., 2004. Seiche characteristics of Rotterdam Harbour. Coastal Engineering 51 (5-6), 373-386.

Dong, G., Gao, J., Ma, X., Wang, G., Ma, Y., 2013. Numerical study of low-frequency waves during harbor resonance. Ocean Engineering 68, 38-46.

Dong, G., Wang, G., Ma, X., Ma, Y., 2010. Harbor resonance induced by subaerial landslide-generated impact waves. Ocean Engineering 37 (10), 927-934.

Dongeren, A.V., Lowe, R., Pomeroy, A., Trang, D.M., Roelvink, D., Symonds, G., Ranasinghe, R., 2013. Numerical modeling of low-frequency wave dynamics over a fringing coral reef. Coastal Engineering 73, 178-190.

Fabrikant, A.L., 1995. Harbor oscillations generated by shear flow. Journal of Fluid Mechanics 282, 203-217.

Gao, J., Ji, C., Gaidai, O., Liu, Y., 2016a. Numerical study of infragravity waves amplification during harbor resonance. Ocean Engineering 116, 90-100.

Gao, J., Ji, C., Gaidai, O., Liu, Y., Ma, X., 2017a. Numerical investigation of transient harbor oscillations induced by N-waves. Coastal Engineering 125, 119-131.

Gao, J., Ji, C., Liu, Y., Gaidai, O., Ma, X., Liu, Z., 2016b. Numerical study on transient harbor oscillations induced by solitary waves. Ocean Engineering 126, 467-480.

Gao, J., Ji, C., Liu, Y., Ma, X., Gaidai, O., 2017b. Influence of offshore topography on the amplification of infragravity oscillations within a harbor. Applied Ocean Research 65, 129-141.

Gao, J., Ji, C., Liu, Y., Ma, X., Gaidai, O., 2018a. Numerical study on transient harbor oscillations induced by successive solitary waves. Ocean Dynamics 68 (2), 193-209.

Gao, J., Ji, C., Ma, X., Liu, Y., Gaidai, O., 2017c. Numerical investigation of infragravity wave amplifications during harbor oscillations influenced by variable offshore topography. Ocean Dynamics 67 (9), 1151-1162.

Gao, J., Ma, X., Dong, G., Wang, G., Ma, Y., 2015. Improvements on the normal mode decomposition method used in harbor resonance. Proc IMechE Part M: Journal of Engineering for the Maritime Environment 229 (4), 397-410.

Gao, J., Ma, X., Dong, G., Wang, G., Ma, Y., 2016c. Numerical study of transient harbor resonance induced by solitary waves. Proc IMechE Part M: Journal of Engineering for the Maritime Environment 230 (1), 163–176.

Gao, J., Zhou, X., Zang, J., Chen, Q., Zhou, L., 2018b. Influence of offshore fringing reefs on infragravity period oscillations within a harbor. Ocean Engineering 158, 286-298.

Gao, J., Zhou, X., Zhou, L., Zang, J., Chen, H., 2019. Numerical investigation on effects of fringing reefs on low-frequency oscillations within a harbor. Ocean Engineering 172, 86-95.

Gao, J., Zhou, X., Zhou, L., Zang, J., Chen, Q., Ding, H., 2018c. Numerical study of harbor oscillations induced by water surface disturbances within harbors of constant depth. Ocean

Dynamics 68 (12), 1663–1681.

Kennedy, A.B., Kirby, J.T., Chen, Q., Dalrymple, R.A., 2001. Boussinesq-type equations with improved nonlinear performance. Wave Motion 33, 225-243.

Kumar, P., Gulshan, 2018. Theoretical analysis of extreme wave oscillation in Paradip Port using a 3-D boundary element method. Ocean Engineering 164, 13-22.

Kumar, P., Zhang, H., Kim, K.I., Yuen, D.A., 2016. Modeling wave and spectral characteristics of moored ship motion in Pohang New Harbor under the resonance conditions. Ocean Engineering 119, 101-113.

López, M., Iglesias, G., 2014. Long wave effects on a vessel at berth. Applied Ocean Research 47, 63-72.

Lee, J.J., 1971. Wave induced oscillations in harbors of arbitrary geometry. Journal of Fluid Mechanics 45, 375-394.

Lepelletier, T.G., Raichlen, F., 1987. Harbor oscillations induced by nonlinear transient long waves. Journal of Waterway, Port, Coastal and Ocean Engineering 113 (4), 381-400.

Liu, P.L.-F., Monserrat, S., Marcos, M., Rabinovich, A.B., 2003. Coupling between two inlets: Observation and modeling. Journal of Geophysical Research: Oceans 108, C3, 3069, doi:10.1029/2002JC001478.

Ma, G., Shi, F., Kirby, J.T., 2012. Shock-capturing non-hydrostatic model for fully dispersive surface wave processes. Ocean Modelling 43-44, 22–35.

Ma, Y., Chen, H., Ma, X., Dong, G., 2017. A numerical investigation on nonlinear transformation of obliquely incident random waves on plane sloping bottoms. Coastal Engineering 130, 65-84.

Madsen, P.A., Fuhrman, D.R., Schäffer, H.A., 2008. On the solitary wave paradigm for tsunamis. Journal of Geophysical Research: Oceans 113, C12012, doi:10.1029/2008JC004932.

Madsen, P.A., Fuhrman, D.R., Wang, B., 2006. A Boussinesq-type method for fully nonlinear waves interacting with a rapidly varying bathymetry. Coastal Engineering 53, 487-504.

Mei, C.C., Agnon, Y., 1989. Long-period oscillations in a harbour induced by incident short waves. Journal of Fluid Mechanics 208, 595-608.

Ning, Y., Liu, W., Sun, Z., Zhao, X., Zhang, Y., 2019. Parametric study of solitary wave propagation and runup over fringing reefs based on a Boussinesq wave model. Journal of Marine Science

and Technology 24 (2), 512–525.

Okihiro, M., Guza, R.T., 1996. Observations of seiche forcing and amplification in three small harbors. Journal of Waterway, Port, Coastal and Ocean Engineering 122 (5), 232-238.

Pattiaratchi, C.B., Wijeratne, E.M.S., 2009. Tide gauge observations of 2004-2007 Indian Ocean tsunamis from Sri Lanka and Western Australia. Pure and Applied Geophysics 166 (1), 233-258.

Shi, F., Kirby, J.T., Harris, J.C., Geiman, J.D., Grilli, S.T., 2012. A high-order adaptive time-stepping TVD solver for Boussinesq modeling of breaking waves and coastal inundation. Ocean Modelling 43-44, 36-51.

Sobey, R.J., 2006. Normal mode decomposition for identification of storm tide and tsunami hazard. Coastal Engineering 53, 289-301.

Su, S.-F., Ma, G., Hsu, T.-W., 2015. Boussinesq modeling of spatial variability of infragravity waves on fringing reefs. Ocean Engineering 101, 78-92.

Suh, K.D., Lee, C., Park, W.S., 1997. Time-dependent equations for wave propagation on rapidly varying topography. Coastal Engineering 32 (2-3), 91-117.

Thotagamuwage, D.T., Pattiaratchi, C.B., 2014a. Influence of offshore topography on infragravity period oscillations in Two Rocks Marina, Western Australia. Coastal Engineering 91, 220-230.

Thotagamuwage, D.T., Pattiaratchi, C.B., 2014b. Observations of infragravity period oscillations in a small marina. Ocean Engineering 88, 435-445.

Vanoni, V.A., Carr, J.H., 1950. Harbor surging, Proceedings of the 1st International Conference on Coastal Engineering, Long Beach, pp. 60-68.

Wang, G., Zheng, J.-H., Maa, J.P.-Y., Zhang, J.-S., Tao, A.-F., 2013. Numerical experiments on transverse oscillations induced by normal-incident waves in a rectangular harbor of constant slope. Ocean Engineering 57, 1-10.

Wang, G., Zheng, J., Liang, Q., Zheng, Y., 2014. Analytical solutions for oscillations in a harbor with a hyperbolic-cosine squared bottom. Ocean Engineering 83, 16-23.

Yao, Y., Becker, J.M., Ford, M.R., Merrifield, M.A., 2016. Modeling wave processes over fringing reefs with an excavation pit. Coastal Engineering 109, 9-19.

Yao, Y., Huang, Z., Monismith, S.G., Lo, E.Y.M., 2012. 1DH Boussinesq modeling of wave transformation over fringing reefs. Ocean Engineering 47, 30-42.

Zhao, X., Wang, B., Liu, H., 2012. Characteristics of tsunami motion and energy budget during runup and rundown processes over a plane beach. Physics of Fluids 24 (6), 062107.